INL/RPT-23-73822

Milestone 1.2.14: Surface Characterization of Irradiated Surrogate Non-Native Corrosion Plumes on Aluminum 6061-T6 Specimens

July 2023

Jacy K. Conrad, Corey D. Pilgrim, Xiaofei Pu, Fidelma Giulia Di Lemma, Fei Xu, James W. Jones, Timothy S. Yoder, Rebecca E. Smith, and Gregory P. Holmbeck

Idaho National Laboratory, Center for Radiation Chemistry Research

Idaho National Laboratory

INL is a U.S. Department of Energy National Laboratory operated by Batelle Energy Alliance, LLC

INL/RPT-23-73822

Milestone 1.2.14: Surface Characterization of Irradiated Surrogate Non-Native Corrosion Plumes on Aluminum 6061-T6 Specimens

Jacy K. Conrad, Corey D. Pilgrim, Xiaofei Pu, Fidelma Giulia Di Lemma, Fei Xu, James W. Jones, Timothy S. Yoder, Rebecca E. Smith, and Gregory P. Holmbeck
Idaho National Laboratory, Center for Radiation Chemistry Research

March 2023

Idaho National Laboratory
Center for Radiation Chemistry Research
Idaho Falls, Idaho, 83415

http://www.inl.gov

Prepared for the
U.S. Department of Energy
Office of Environmental Management
Under DOE Idaho Operations Office
Contract DE-AC07-05ID14517

ABSTRACT

The United States Department of Energy is seeking to evaluate the feasibility of extended dry storage of aluminum-clad spent nuclear fuel (ASNF) in helium-backfilled cannisters. A significant research effort has been devoted to determining the amount of radiation-induced molecular hydrogen generation from corrosion layers that would be present on the fuel assembly surfaces. However, to date, no evidence of radiation-induced changes in the microstructure of the corroded aluminum surfaces have been reported. This report provides surface characterization, in terms of corrosion layer composition and morphology, for aluminum alloy 6061-T6 "plume" samples subjected to one of three potential ASNF drying techniques—"*vacuum only*", "*vacuum + 4 hours at 100 ^{o}C*", and "*vacuum + 4 hours at 220 ^{o}C*"—and gamma irradiated (≤ 53 MGy) in the presence of helium gas with ~0% added relative humidity. At these high absorbed gamma doses, for the first time ever, radiation-induced circular defects were found on the sample surface, regardless of the drying regime employed. Additionally, large cracks that penetrated through the corrosion layer to expose bare aluminum metal were observed in irradiated "plume" specimens subjected to drying conditions of "*vacuum + 4 hours at 220 ^{o}C*". The nature and implications of these defects on the extended dry storage of ASNF is unclear, requiring further study.

CONTENTS

ACRONYMS

AA1100	Aluminum alloy 1100
AA6061	Aluminum alloy 6061
Al···$OH^{\bullet}$	Aluminum surface bound hydroxyl radical
Al···OH^{-}	Aluminum surface bound hydroxide group
Al···OH_2	Aluminum surface bound water
Al···$O^{\bullet -}$	Aluminum surface bound oxygen radical anion
Al(s)	Aluminum metal
ASNF	Aluminum-clad spent nuclear fuel
ATR	Advanced Test Reactor
BSE	Backscattered-electron
CR2	Center for Radiation Chemistry Research
DOE	Department of Energy
e^{-}	Electron
EDS	Energy dispersive X-ray spectroscopy
h^{+}	Electron vacancy hole
$H^{\bullet}$	Hydrogen atom
H_2	Molecular hydrogen gas
$H_2O^{\bullet +}$	Water radical cation
He	Helium gas
INL	Idaho National Laboratory
PAS	Positron annihilation spectroscopy
RH	Relative humidity
SEM	Scanning electron microscopy
U.S.	United States
XRD	X-ray diffraction

1. INTRODUCTION

A technical basis for the dry storage of aluminum-clad spent nuclear fuel (ASNF) in helium-backfilled cannisters over extended time periods (> 50 years) has been investigated.[1] Studies within this initiative have proven to be essential for the development of predictive computer models for the behavior of these ASNF systems over the anticipated storage period.[2–6] One area of particular focus was the potential for the radiolytic production of molecular hydrogen gas (H_2) from aluminum corrosion layers, due to the radioactive nature of ASNF.[7–13] Generation of excessive H_2 could potentially impact the longevity and safety of storing ASNF in the standard U.S. Department of Energy (DOE) canister[14–16] owing to alloy embrittlement, cannister pressurization, and/or the formation of potentially flammable gaseous mixtures.[17–20]

Corrosion of aluminum metal alloys produces a mixture of aluminum oxide, hydroxide, and oxy-hydroxide polymorphs on the metal surface. Radiolytic H_2 generation is known to occur on corroded ASNF surfaces, and a few key mechanisms have been proposed for radiation-induced formation of H_2 from these systems. Initially, an electron (e^-) and hole (h^+) pair are generated in the solid from the absorption of ionizing radiation.[21] The hole can take the form of a water radical cation ($H_2O^{\bullet+}$) chemisorbed or physisorbed on the corrosion layer surface, which can dissociatively recombine with an electron to form an excited state that breaks apart to yield H_2:[22]

$$Al\cdots H_2O^{\bullet+} + e^- \rightarrow Al\cdots H_2O^* \rightarrow H_2 + Al\cdots O^{\bullet}. \quad (1)$$

Alternatively, surface adsorbed water can undergo dissociative electron attachment, yielding surface bound hydroxyl anions ($Al\cdots OH^-$) and hydrogen atoms ($H^{\bullet}$):

$$Al\cdots H_2O + e^- \rightarrow H^{\bullet} + Al\cdots OH^-. \quad (2)$$

There is also the possibility of the direct interaction of radiation with the hydroxyl groups connecting the hydroxide or oxyhydroxide crystal lattices, leading to ionization with bound oxygen-centered radical species as a product:[23,24]

$$Al\cdots OH^- \rightsquigarrow Al\cdots OH^{\bullet} + e^- \rightarrow Al\cdots O^{\bullet-} + H^{\bullet}, \quad (3)$$

or homolytic dissociation mechanisms:[23,24]

$$Al\cdots OH^- \rightsquigarrow Al\cdots O^{\bullet-} + H^{\bullet}. \quad (4)$$

The extent of dissociation is increased when a hole is formed at the site of an oxygen atom, as it weakens the O–H bond.[25] The $H^{\bullet}$ atoms that are generated in **Eq. 2–4** can also initiate secondary indirect radiation effects, tending to combine with themselves or remove other hydrogen atoms from nearby surface-adsorbed water or hydroxyl groups to yield H_2:[12,13,21,24,26]

$$H^{\bullet} + H^{\bullet} \rightarrow H_2, \quad (5)$$

$$H^{\bullet} + Al\cdots OH_2 \rightarrow H_2 + Al\cdots OH^{\bullet}, \quad (6)$$

$$H^{\bullet} + Al\cdots OH^- \rightarrow H_2 + Al\cdots O^{\bullet-}. \quad (7)$$

The overall H_2 generated from these systems has been shown to initially increase with absorbed gamma radiation dose, with the overall yield depending on the particular aluminum alloy, relative humidity (RH), temperature, and backfill gaseous environment.[12,13] The radiolytic yield of H_2—*G*-value—eventually reaches a steady-state value as the precursors for H_2 generation are gradually depleted by the above radiation-induced processes, and the H_2 generated begins to participate in further radiolytic and surface-catalyzed reactions, such as:[27,28]

$$H_2 \rightsquigarrow H^{\bullet}, H_2^+, e^-, \quad (8)$$

$$H_2 + Al\cdots O^{\bullet-} \rightarrow Al\cdots OH^- + H^{\bullet}, \quad (9)$$

$$H^{\bullet} + Al\cdots OH \rightarrow Al(s) + H_2O, \quad (10)$$

$$H_2 + Al(s) \rightarrow Al(s) + H^{\bullet} + H^{\bullet} \text{ (homolytic)}, \quad (11)$$

$$H_2 + Al(s) \rightarrow Al(s) + H^- + H^+ \text{ (heterolytic)}. \quad (12)$$

Consequently, understanding the factors that affect the steady-state yield of H_2 is critical for the development and validation of accurate predictive models to support the safe, extended dry-storage of ASNF.[2–6]

With this goal in mind, our most recent ASNF irradiation study evaluated the impact of non-native corrosion "plumes" on the steady-state yield of H_2,[29] owing to the observation of similar plumes during the inspection of Advanced Test Reactor (ATR) ASNF elements.[30] These plumes have been attributed to damage of the initial passivated corrosion layer during post-reactor operation manipulations. Once damaged, subsequent water-mediated ambient-temperature-corrosion processes are believed to have occurred in the ATR cooling canal and Chemical Processing Plant 603 basin.[30] The result of these ambient-temperature-corrosion processes is a much thicker (> 6 µm) aluminum corrosion layer, as compared with the initial passivated corrosion layer (2–6 µm). Our study found that similar amounts of H_2 were formed from the gamma irradiated surrogate non-native corrosion "plume" samples of aluminum alloy 6061-T6 (AA6061-T6), as compared with values from previously irradiated high-temperature-corroded AA6061-T6 coupons, as shown in **Fig. 1**.[13]

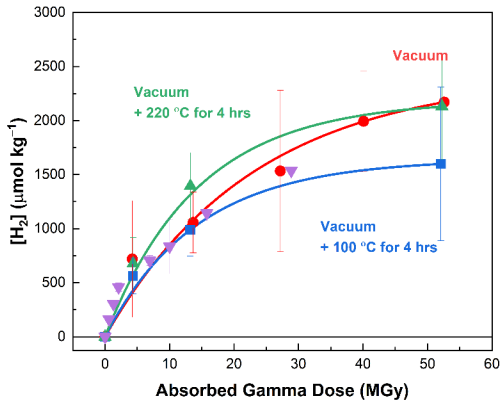

Fig. 1. Concentration of H_2 generated in helium (He) environments as a function of absorbed gamma dose from the irradiation of high temperature corroded AA6061-T6 coupons with ~50% added relative humidity (RH) dried in air (❑) and ambient temperature corroded AA6061-T6 plates with ~0% added RH for each drying condition: vacuum drying only (ᔓ); vacuum drying + 100 °C heating for 4 hr (O); and vacuum drying + 220 °C heating for 4 hr (❑). Solid curves are exponential fits to the data. Figure reproduced from reference 29

Knowledge of potential changes in the surface morphology with irradiation and their implications is essential for the safe manipulation, storage, and management of ASNF. To date, the surfaces of these irradiated "plume" samples have not been interrogated. Previous studies in this area have reported no change in the vibrational spectra of aluminum oxyhydroxide or hydroxide powders up to absorbed gamma doses of 120 kGy.[9] Similarly, no structural changes were seen in these same irradiated powders using infrared, Raman, and *X*-ray diffraction (XRD) spectroscopies up to 2 MGy of absorbed gamma dose.[31,32] These results are expected since gamma radiation-induced damage is primarily instigated by secondary electrons, which are very low in mass, and therefore do not have the momentum to displace atoms/ions and alter a material's structure. Alpha particles, on the other hand, do have sufficient mass to impart ballistic displacement damage and deposit a large amount of energy per unit volume traversed.[31] However, alpha particle irradiation—in the form of accelerated helium ions—of boehmite and gibbsite powders afforded no observable changes in either material's crystal structure up to 175 MGy, as probed by Raman spectroscopy and XRD.[31]

That said, here we report the first ever finding of gamma radiation-induced surface defects/damage arising from the long-term irradiation (≤ 53 MGy) of the aforementioned AA6061-T6 "plume" samples, pretreated with one of three proposed ASNF drying techniques[33–35]—"*vacuum only*", "*vacuum + 4 hours at 100 °C*", and "*vacuum + 4 hours at 220 °C*"—and sealed in helium gas (He) environments with ~0% added relative humidity (RH).

2. EXPERIMENTAL METHODS

2.1. Materials

AA6061-T6 plates (3.15 in. × 12 in. × 0.050 in., with six ¼ in. diameter holes for mounting) were sourced from QLab Corporation (Westlake, Ohio, USA) in the as-milled surface condition. The preparation, ambient-temperature-corrosion, and drying procedures for the fabrication of AA6061-T6 coupon samples from a single AA6061-T6 plate was as previously reported.[29] Acetone (HPLC Plus, ≥ 99.9%) and ethanol (absolute, ≥ 99.8%) were supplied by MilliporeSigma. Helium was purchased in its highest available purity from Norco. Ultra-pure water (18.2 MΩ·cm) was generated in-house using a ThermoScientific (Waltham, MA, USA) Harvey™ DI+ Cartridge System, and used for all water applications. Unless otherwise stated, all materials were used as received.

2.2. Steady-State Gamma Irradiations

Gamma irradiations were performed using the Idaho National Laboratory (INL) Center for Radiation Chemistry Research (CR2) Foss Therapy Services (Pacoima, California, USA) Model 812 cobalt-60 gamma irradiator. Corroded AA6061-T6 coupons were dried using one of three proposed drying strategies—"*vacuum only*", "*vacuum + 4 hours at 100 °C*", and "*vacuum + 4 hours at 220 °C*"—and then individually flame-sealed in borosilicate glass ampules backfilled with helium and ~0% added RH prior to being loaded into the irradiator. These flame-sealed samples were irradiated for ~250 days under ambient irradiator temperature (~40 °C) conditions. Chemical dosimetry via Fricke solution[36] was used to determine the dose rate (65–456 Gy min^{-1}) at each occupied sample position in the gamma irradiator. Measured dose rates were then corrected for the natural decay of the cobalt-60 sources ($\tau_{1/2}$ = 5.27 years) and for the electron density difference between aluminum metal and water (0.8673).[12,13] Post irradiation, the sample glass ampules were crushed for head space gas analysis[29] and for the recovery of the irradiated coupon for surface characterization.

2.3. Surface Characterization

Corrosion layer composition and morphology was evaluated using XRD and scanning electron microscopy (SEM) with energy dispersive X-ray spectroscopy (EDS) techniques pre- and post-irradiation to identify correlations with the previously reported steady-state H_2 yields.[29]

The XRD data was measured using a Malvern Panalytical (Malvern, The Netherlands) Empyrean X-ray Diffractometer at the INL Irradiated Materials Characterization Laboratory, located in the Materials and Fuels Complex. The XRD analyses were performed in the Bragg-Brentano geometry, with a copper K_α X-ray beam at 45 kV and 40 mA, and a PIXEL-3D detector. AA6061-T6 coupon samples were loaded onto a zero-background plate to reduce signal interference. The XRD results represent bulk analysis from the entirety of the sample surface, as the beam size was larger than the coupons used in this work. The measured 2-theta angles ranged from 10 to 90 degrees and were collected in continuous scan mode with a scanning step size of 0.026 degrees and a counting time of 200 seconds per step. The data were analyzed using *HighScore* software and compared against the ICDD PDF 4+ 2021 database for phase identification.[37]

The SEM/EDS data were collected using a JEOL (Peabody, Massachusetts, USA) IT-500-HR, equipped with an Oxford EDS Ultimax-65 for elemental analysis to characterize sample morphology and, by using cross-sectional cuts, examine the extent of surface corrosion penetration into the bulk material. SEM/EDS analyses were performed at an accelerating voltage of 15–20 keV, with the current optimized to obtain < 50% deadtime. X-ray maps were collected with a with a resolution of 512 × 384 pixels and a dwell time of 100 ms for a total of at least 10 frames. EDS analyses were performed using the standardless method in which the relative peak intensities are used to identify the ratio of elements rather than a physical standard. Images were collected in secondary-electron mode for morphological information and in backscattered-electron (BSE) mode for compositional information.

3. RESULTS AND DISCUSSION

The AA6061-T6 "plume" samples investigated by this work exhibited more uniform corrosion layers as compared with high-temperature-corroded (30 days at 95 °C) aluminum coupons,[12] and consisted entirely of the bayerite phase, as shown by the XRD diffractograms for the non-irradiated and ~52 MGy samples from each drying condition in **Fig. 2**.

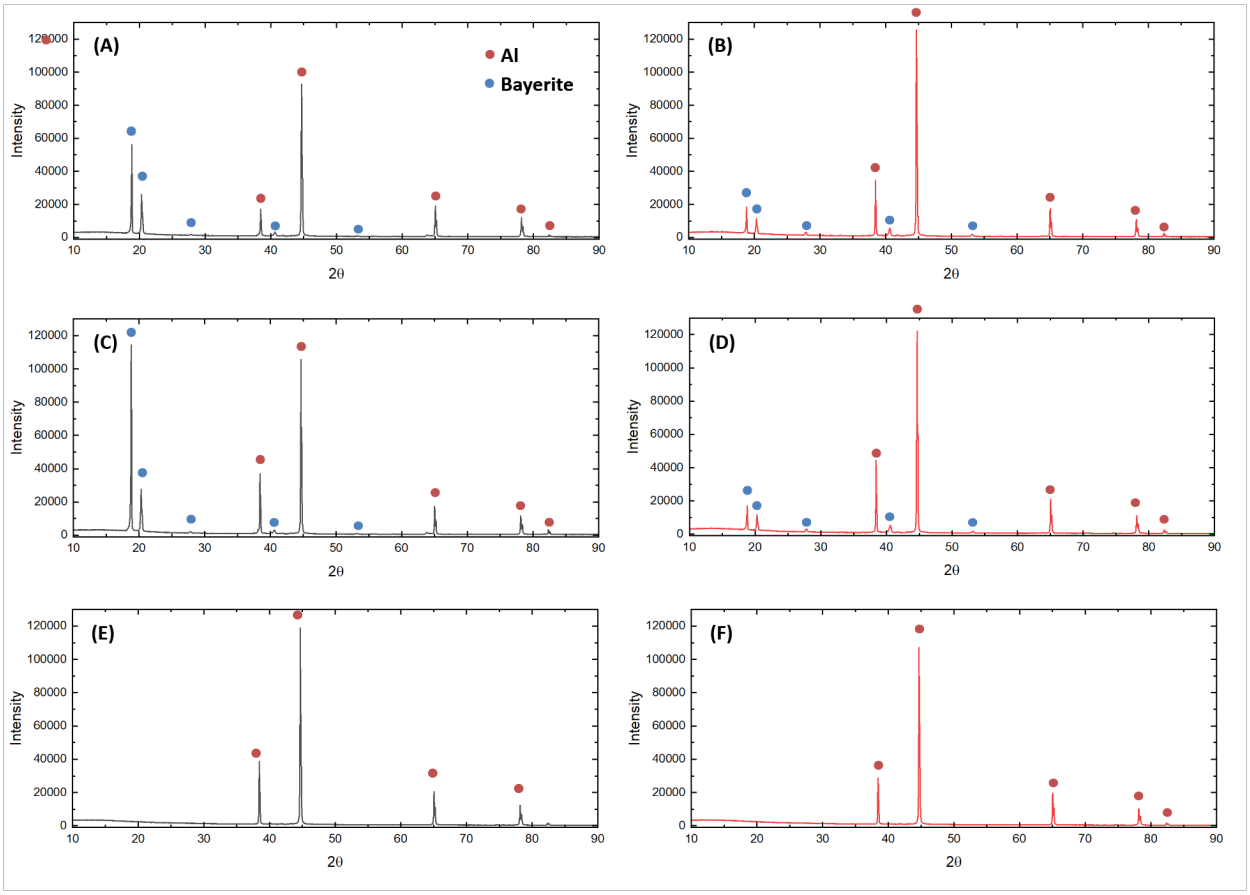

Fig. 1. XRD patterns for ambient-temperature-corroded AA6061-T6 "plume" coupons under: "*vacuum only*" non-irradiated **(A)** and gamma irradiated to 52.6 MGy **(B)** conditions; "*vacuum + 4 hours at 100 °C*" non-irradiated **(C)** and gamma irradiated to 52.1 MGy **(D)** conditions; and "*vacuum + 4 hours at 220 °C*" non-irradiated **(E)** and gamma irradiated to 52.2 MGy **(F)** conditions.

No significant differences in the distribution of aluminum polymorphs were observed between the "*vacuum only*" and the "*vacuum + 100 °C for 4 hr*" drying treatments, although the bayerite phase was entirely gone under the "*vacuum + 220 °C for 4 hr"* condition. We have previously shown that the removal of chemisorbed water is not the only effect promoted at 220 °C, and therefore expected a change. A significant increase in H_2 formation was observed from the gamma irradiation of high-temperature-corroded AA1100 coupons at 200 °C in our previous work.[12] This phenomena was attributed to a combination of: (i) the dehydration of bayerite to pseudo-boehmite, boehmite, and ultimately alumina—a polymorph transformation process that begins above ~120 °C;[38–40] and (ii) more efficient release of H• atoms and H_2 through annealing.[9] Dehydroxylation of various aluminum polymorphs has been studied in the past and generally results in the formation of alumina at temperatures > 250 °C. Interestingly, there was no boehmite or alumina seen for the coupons dried at 220 °C. In fact, quite surprisingly, no oxidized form of aluminum was seen at all under this drying condition. Overall, the surface effects induced by the various drying treatments are at odds to their impact on the steady-state yield of H_2, for which negligible

difference was found, as shown in **Fig. 1**.[29] In all cases, gamma irradiations to ~52 MGy had no impact on the XRD diffractograms in **Fig. 2**.

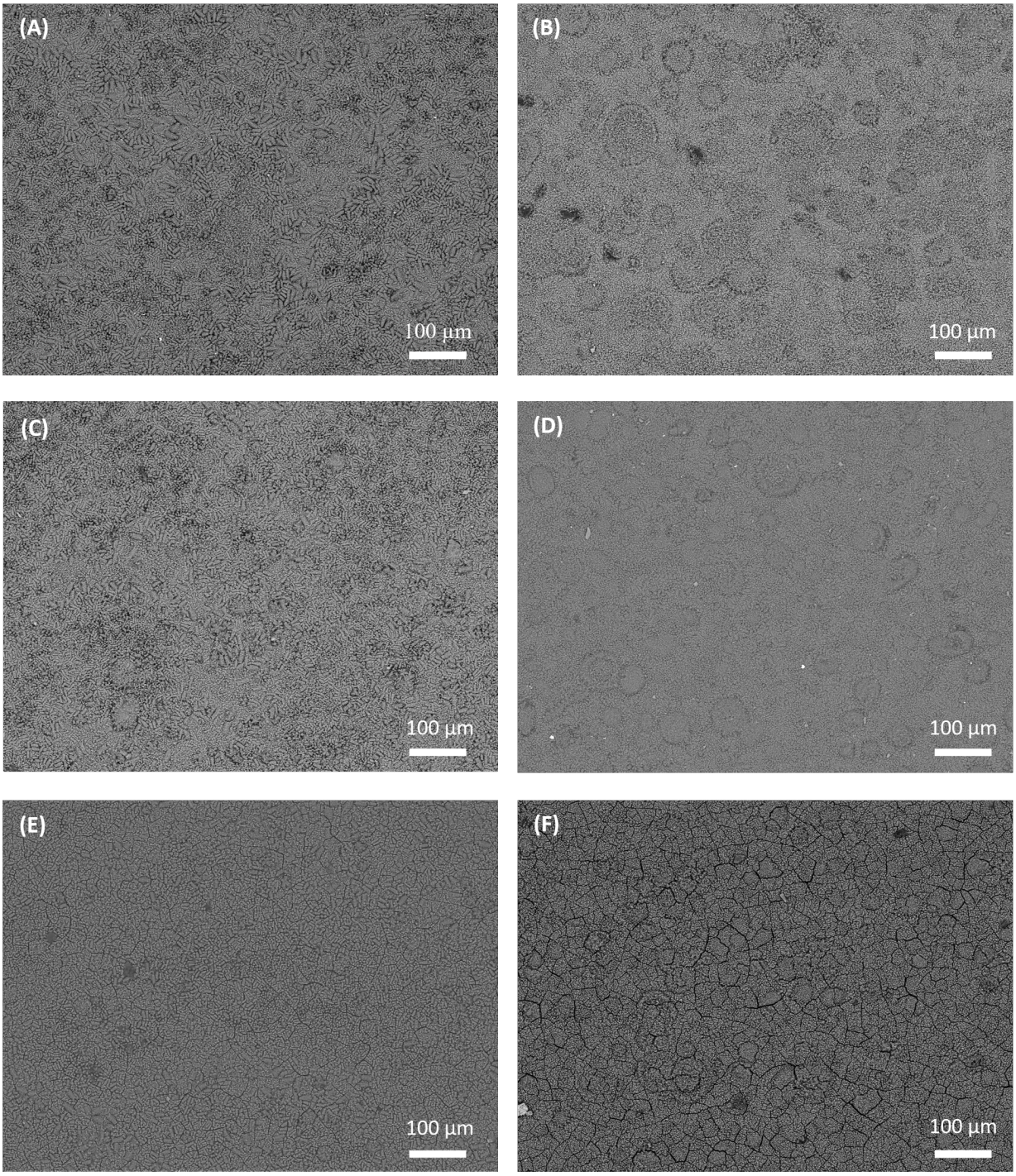

Fig. 2. SEM micrographs, with 100 µm scale bars, of the upper surface of the ambient-temperature-corroded AA6061-T6 "plume" coupons under: "*vacuum only*" non-irradiated **(A)** and gamma irradiated to 52.6 MGy **(B)** conditions; "*vacuum + 4 hours at 100 °C*" non-irradiated **(C)** and gamma irradiated to 52.1 MGy **(D)** conditions; and "*vacuum + 4 hours at 220 °C*" non-irradiated **(E)** and gamma irradiated to 52.2 MGy **(F)** conditions.

The corresponding SEM micrographs for the "plume" specimens are shown in **Fig. 3** for non-irradiated and ~52 MGy samples for all three drying procedures. The surface morphology of the samples dried under "*vacuum only*" and "*vacuum + 4 hours at 100 °C*" conditions are indistinguishable from one another, and both show rod-like microstructures across their surface. The "*vacuum + 4 hours at 220 °C*" specimens on the other hand, have a markedly different appearance, exhibiting large cracks on the surface.

Circular features with diameters on the order of 20–100 μm were also observed on the irradiated "plume" coupon surfaces for all three drying conditions, albeit they are more difficult to see for the "*vacuum + 4 hours at 220 °C*" specimens. These defects were not present prior to irradiation, nor observed in our previous high-temperature-corrosion studies.[12,13] These are the first evidence of defects, or other radiation-induced damage, to corroded aluminum coupons by gamma radiation that we have observed, or that have been reported in the literature. The nature and implications of these defects on the extended dry storage of ASNF are unclear, and thus require further study.

Elemental mapping of the "plume" sample surfaces using EDS showed no obvious differences between the different drying regimes, nor were there any detectable changes in composition or elemental distribution around the circular features associated with the aforementioned gamma radiation-induced damage. EDS micrographs for images from a representative area for each drying condition are given in **Fig. 4–6**, where the lack of elemental features is apparent. Further investigations into the nature of these circular features are underway using Positron Annihilation Spectroscopy (PAS), which has been demonstrated to be capable of identifying lattice defects; precipitates; mono-, bi-, and poly-vacancies; vacancy clusters; and voids while quantifying their respective concentrations in nuclear materials irradiated using neutron and/or ion bombardment.[41]

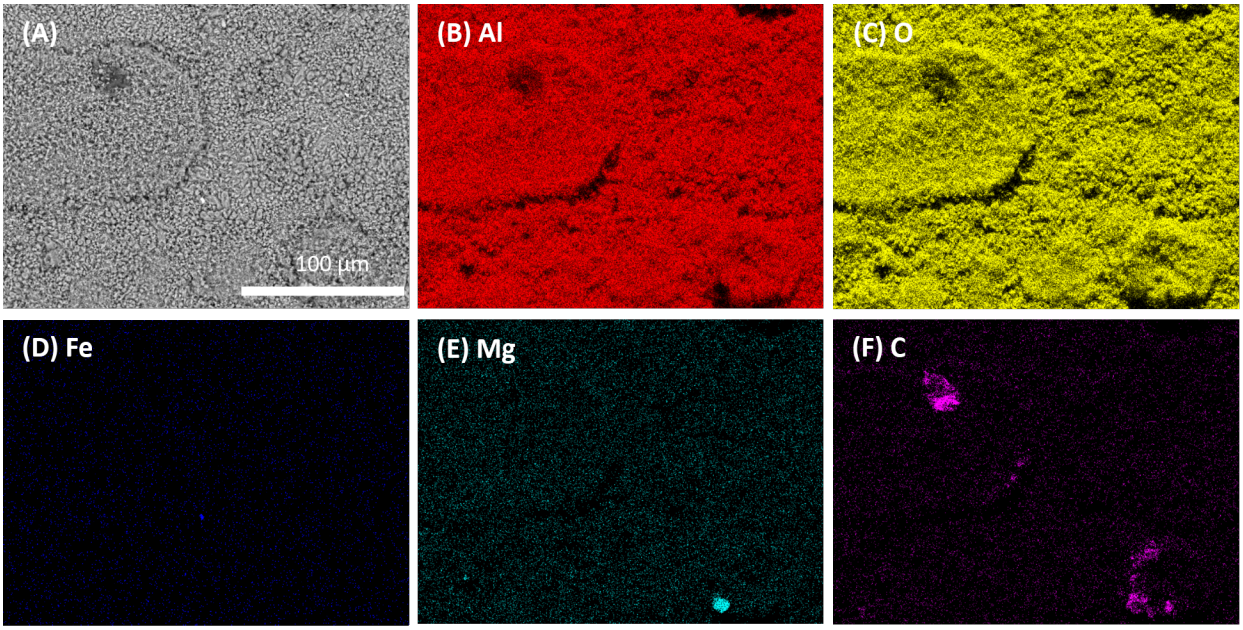

Fig. 3. (A) SEM micrograph of a corroded AA6061-T6 "plume" coupon surface dried under "*vacuum only*" and irradiated to 52.6 MGy, and the corresponding EDS elemental maps for aluminum (Al, **B**), oxygen (O, **C**), iron (Fe, **D**), magnesium (Mg, **E**) and carbon (C, **F**).

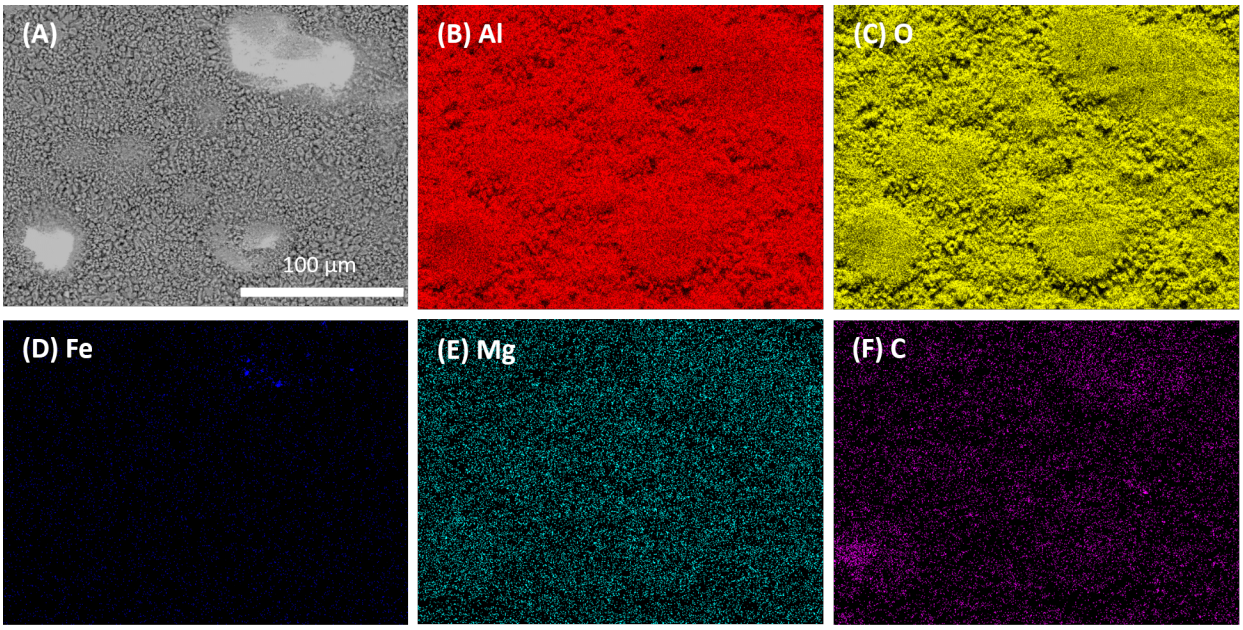

Fig. 4. (A) SEM micrograph of a corroded AA6061-T6 "plume" coupon surface dried under "*vacuum only + 4 hours at 100 °C*" and irradiated to 52.1 MGy, and the corresponding EDS elemental maps for aluminum (Al, **B**), oxygen (O, **C**), iron (Fe, **D**), magnesium (Mg, **E**) and carbon (C, **F**).

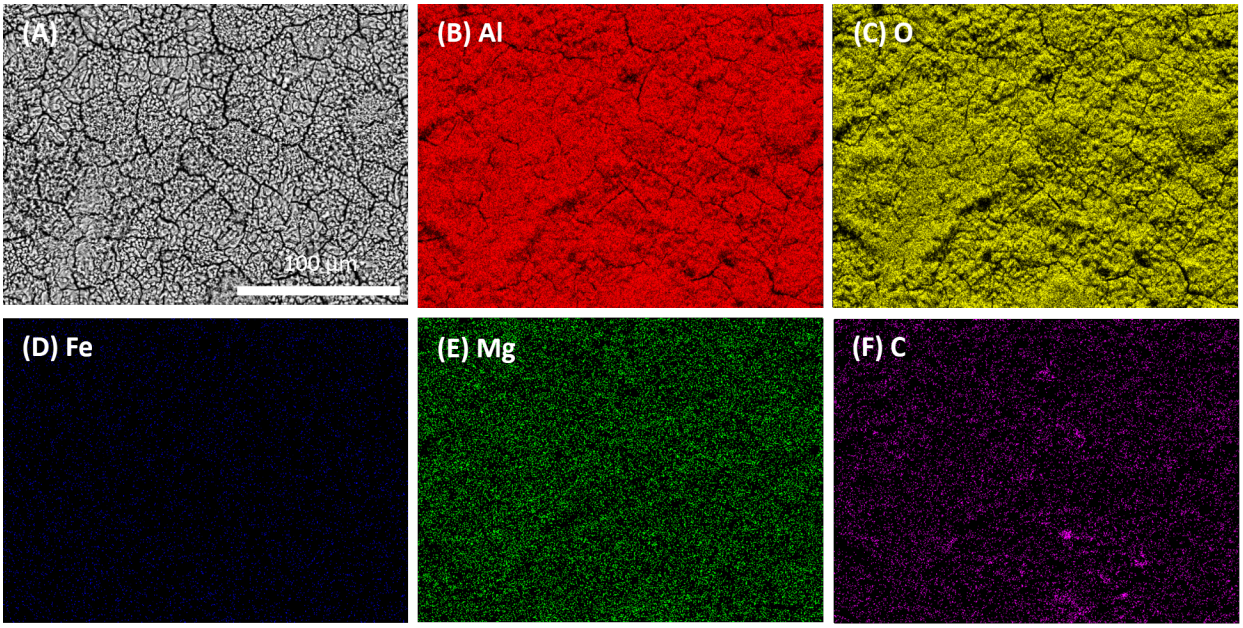

Fig. 5. (A) SEM micrograph of a corroded AA6061-T6 "plume" coupon surface dried under "*vacuum only + 4 hours at 220 °C*" and irradiated to 52.2 MGy, and the corresponding EDS elemental maps for aluminum (Al, **B**), oxygen (O, **C**), iron (Fe, **D**), magnesium (Mg, **E**) and carbon (C, **F**).

Cross-sectional SEM micrographs were also obtained for these samples to examine the depth of the corrosion layer for each drying condition and to see if this layer changed after ~52 MGy of absorbed gamma dose. An example cross-sectional micrograph showing the corrosion layer thickness calculation is given in **Fig. 7**. The micrographs are grayscale images with the value of each pixel (the smallest element in digital image) having an intensity between [0,255], where the brighter region in the image has the

higher intensity value. The cross-section shows three distinct regions with different intensity ranges where the dark area on top, indicated by the green arrow in **Fig. 7 (a)** is the epoxy mounting material, the central medium gray area indicated by the red arrow is the corrosion layer, and the lighter gray area on the bottom indicated by the blue arrow is the aluminum metal. Based on this observation, the average corrosion layer thickness on the cross-sectional samples were determined by a multiple threshold segmentation method[44] by clustering the intensities into these three groups. After this process, manual morphological operations were employed to remove the anomalies in the corrosion layer as shown by the yellow circles in **Fig. 7 (a)**. The corrosion detection result is shown in **Fig. 7 (b)**. To measure the corrosion thickness, we generated the upper boundary and lower boundary separately, and computed the minimum Euclidean distances as the thicknesses between the pairs of two boundaries. The thickness distribution is shown in **Fig. 7 (c)** and the thicknesses of corresponding locations are illustrated in **Fig. 7 (d)**.

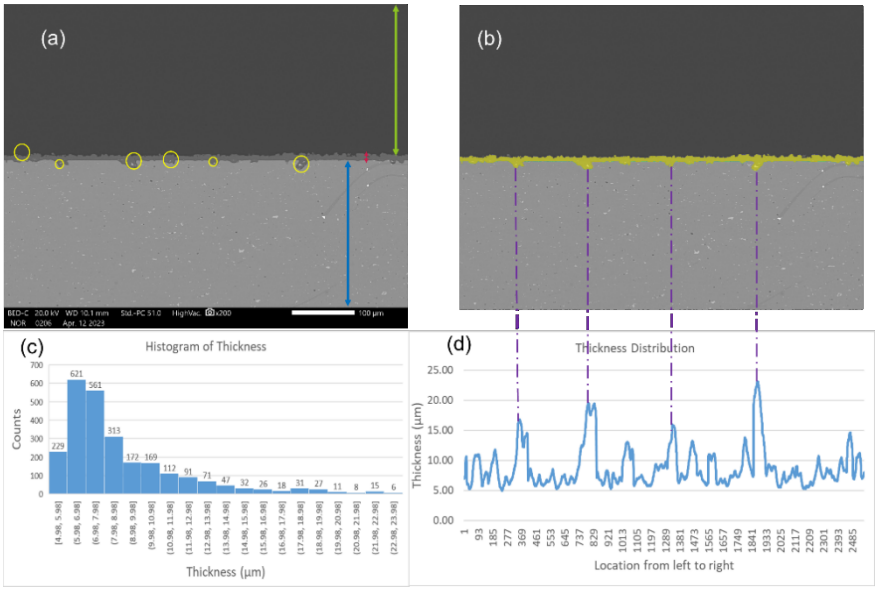

Fig. 6. (a) Original SEM images of a non-irradiated AA6061-T6 "plume" coupon dried under "*vacuum + 4 hours at 100 °C*" with three distinct intensity zones, where the zone indicated by the red arrow is the expected corrosion region. (**b**) Corrosion detection result with yellow color overlayed. (**c**) Histogram of thicknesses at each location. (**d**) Illustration of thicknesses corresponding to locations.

Example micrographs showing the corrosion layers for each drying condition before and after gamma irradiation are given in **Fig. 8** with the average corrosion layer thickness indicated in red font. The overall average corrosion layer thickness was 8 ± 3 μm with no statistically significant difference observed between the different drying procedures, or before and after gamma irradiation. These corrosion layer thicknesses are similar to those reported for the plumes on the ATR ASNF.[30] The cracks that were apparent on the surface of the samples dried under "*vacuum + 4 hours at 220 °C*" are even more obvious in cross-section, where they provide straight channels from the surface down to the aluminum metal. Clearly these samples still have a corrosion layer on their surfaces, despite the XRD analysis not being able to quantify anything beyond metallic aluminum. This observation is made even clearer in the cross-sectional elemental mapping plots, as for the samples dried under "*vacuum + 4 hours at 220 °C*" conditions, shown in **Fig. 9**. Here, as one would expect, aluminum is most concentrated in the base metal layer, as is the magnesium. There are small regions in the base metal where iron is found to be more concentrated than in other areas. The carbon is primarily found in the epoxy on top of the corrosion layer and in the cracks that run through it. The oxygen in these samples is primarily distributed in the corrosion layer, as one would expect for an aluminum oxide, hydroxide, or oxyhydroxide containing phase. Therefore, the cross-sectional EDS demonstrate that an oxide layer is still present after the "*vacuum + 4 hours at 220 °C*" drying treatment. Further investigation is underway to determine why the XRD analysis

was unable to see this oxidized aluminum layer.

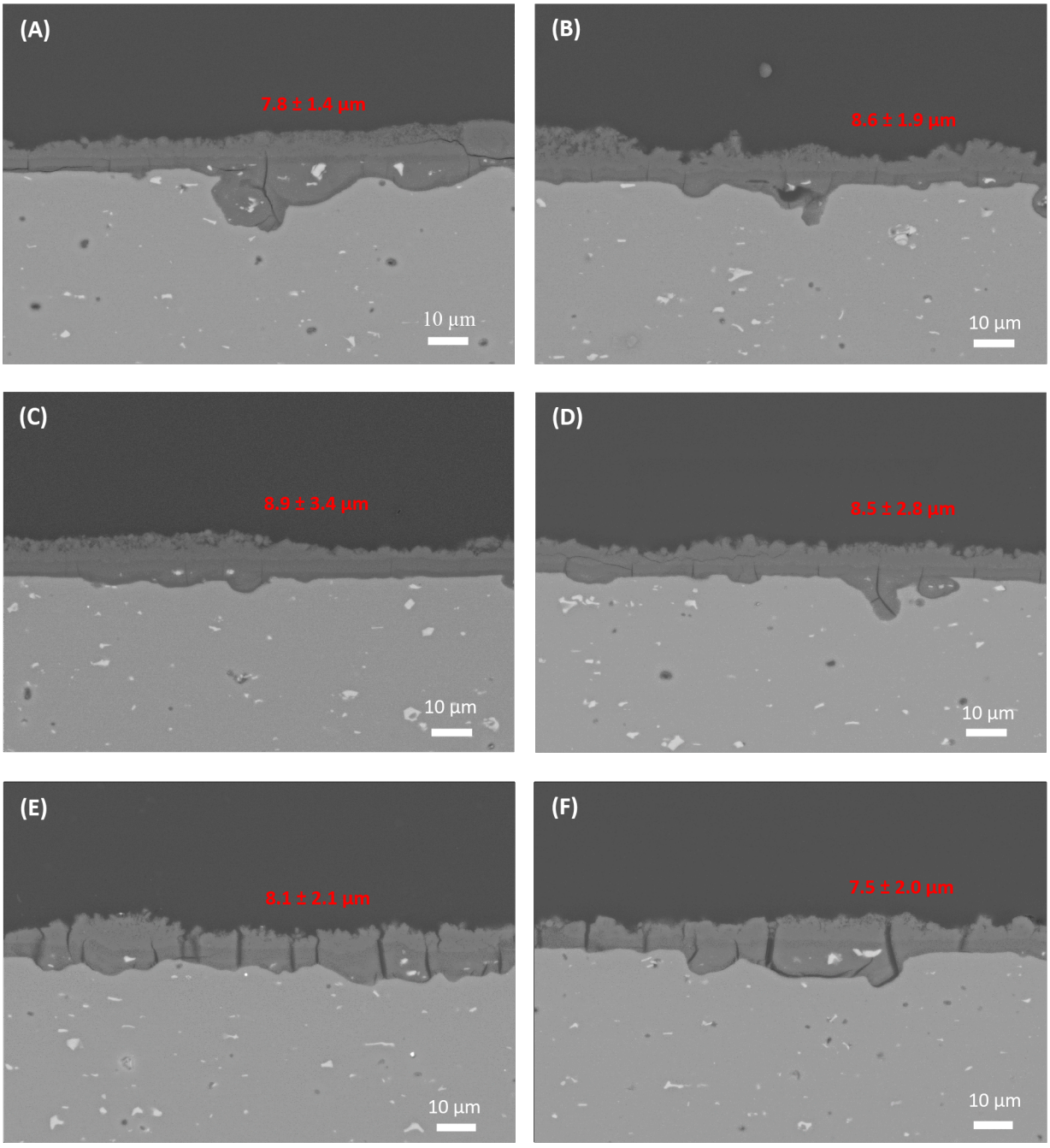

Fig. 7. SEM micrographs, with 10 µm scale bars, of a AA6061-T6 "plume" coupon cross-section under: "*vacuum only*" non-irradiated **(A)** and gamma irradiated to 52.6 MGy **(B)** conditions; "*vacuum + 4 hours at 100 °C*" non-irradiated **(C)** and gamma irradiated to 52.1 MGy **(D)** conditions; and "*vacuum + 4 hours at 220 °C*" non-irradiated **(E)** and gamma irradiated to 52.2 MGy **(F)** conditions. The average corrosion layer thickness is indicated on each micrograph in red font.

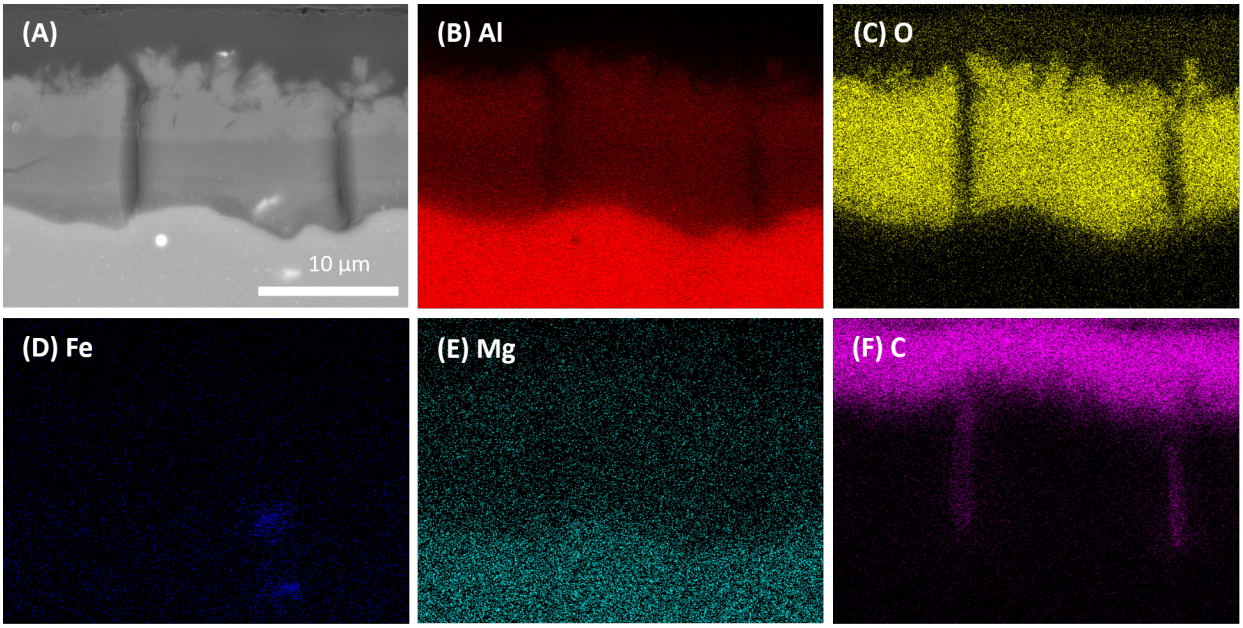

Fig. 8. (A) SEM micrograph of a corroded AA6061-T6 "plume" coupon surface dried under "*vacuum only + 4 hours at 220 °C*" prior to gamma irradiation, and the corresponding EDS elemental maps for aluminum (Al, **B**), oxygen (O, **C**), iron (Fe, **D**), magnesium (Mg, **E**) and carbon (C, **F**).

4. CONCLUSIONS

The aim of this study was to determine whether elevated gamma doses (>2.5 MGy) promoted physical and chemical changes to non-native corrosion plumes on AA6061-T6 coupons, thereby complimenting previously reported radiolytic H_2 production measurements.[29] The presented data shows that the absorption of gamma radiation had no impact on the chemical composition of the corrosion layers present on ambient-temperature-corroded AA6061-T6 "plume" specimens pretreated with any one of the three proposed ASNF drying techniques.

However, we did observe for the first time physical damage to the coupon's surface, irrespective of drying pretreatment regime, in the form of circular features with diameters on the order of 20–100 µm. Furthermore, large cracks were observed in the corrosion layers of irradiated "plume" specimens subjected to drying conditions of "*vacuum + 4 hours at 220 °C*". These radiation-induced cracks were found to penetrate through the corrosion layer to expose bare aluminum metal, potentially facilitating additional, currently unanticipated, chemistries. Overall, the nature and implications of these radiation-induced defects/damage on the extended dry storage of ASNF is unclear and require further study.

5. ACKNOWLEDGMENTS

This work was supported by the U.S. Department of Environmental Management, Office of Technology Development, under contract DE-AC07-05ID14517.

6. REFERENCES

(1) E. Eidelpes, J.J. Jarrell, T.E. Lister, G.P. Horne, E.H. Parker-Quaife, J.K. Conrad, C.D. Pilgrim, A.W. Abboud, P.L. Winston, R.E. Smith, A.L. d'Entremont, B.C. Randall, and R.L. Sindelar, Technical basis for extended dry storage of aluminum-clad spent nuclear fuel. *J. Nucl. Mat.* **2023**, *577*, 154299.

(2) A. Abboud, Modeling Summary of ASNF in DOE Sealed Standard Canisters. *INL EXT-21-64413* **2021**.

(3) A. Abboud, Modeling of Radiolytic Hydrogen Generation of Irradiated Surrogate Aluminum Plates. *INL-RPT-21-66504* **2021**.

(4) A. Abboud, Extended Modeling of DOE Sealed Canisters with Updated Chemistry Models. *INL-RPT-22-67694* **2022**.

(5) A.W. Abboud, Sensitivity study of coupled chemical-CFD simulations for analyzing aluminum-clad spent nuclear fuel storage in sealed canisters. *Nucl. Eng. Des.* **2022**, *390*, 111691.

(6) A.W. Abboud, Modeling DOE Standard Canister Configurations with Updated Surface Chemistry. *INL/RPT-23-73230* **2023**.

(7) D.L. Fisher, L.M. Westbrook, and R.L. Sindelar, Test Results from Gamma Irradiation of Aluminum Oxyhydroxides. Savannah River National Laboratory **2012**.

(8) M.L. Westbrook, R.L. Sindelar, and D.L. Fisher, Radiolytic hydrogen generation from aluminum oxyhydroxide solids: theory and experiment. *J. Radioanal. Nucl. Chem.* **2015**, *303*, 81.

(9) J.A. Kaddissy, S. Esnouf, D. Durand, D. Saffre, E. Foy, J.-P. Renault, Radiolytic Events in Nanostructured Aluminum Hydroxides. *J. Phys. Chem. C* **2017**, *121*, 6365.

(10) S.C. Rieff and J.A. LaVerne, Radiolysis of water with aluminum oxide surfaces. *Rad. Phys. Chem.* **2017**, *131*, 46.

(11) J.A. LaVerne and P.L. Huestis, H Atom Production and Reaction in the Gamma Radiolysis of Thermally Modified Boehmite. *J. Phys. Chem. C* **2019**, *123 (34)*, 21005.

(12) E.H. Parker-Quaife, C. Verst, C.R. Heathman, P.Z. Zalupski, and G.P. Horne, Radiation-Induced Molecular Hydrogen Gas Generation in the Presence of Aluminum Alloy 1100. *Rad. Phys. Chem.* **2020**, *177*, 109117.

(13) J.K. Conrad, A.R. Khanolkar, X. Pu, T.M. Copeland-Johnson, C.D. Pilgrim, J.R. Wilbanks, E.H. Parker-Quaife, and G.P. Horne, Radiolytic Gas Production from Aluminium Coupons (Alloy 1100 and 6061) in Helium Environments – Assessing the Extended Storage of Aluminium Clad Spent Nuclear Fuel. *MDPI Mat.* **2022**, *15*, 7317.

(14) United States Department of Energy, Preliminary Design, Specification for Department of Energy Standardized Spent Nuclear Fuel Canisters. Idaho Falls, Vol I Design Specification, **1998**.

(15) United States Department of Energy, Preliminary Design, Specification for Department of Energy Standardized Spent Nuclear Fuel Canisters. Idaho Falls, Vol II Rationale document, **1998**.

(16) S. Snow, ECAR 4632, Supplemental Evaluation of the DOE Standard SNF Canister for Accidental Drops, **2019**.

(17) R. Ambat and E.S. Dwaarakadasa, Effect of hydrogen in aluminium and aluminium alloys: a review. *Bull. Mater. Sci.* **1996**, *19*, 103.

(18) R.P. Gangloff and B.P. Somerday, Gaseous Hydrogen Embrittlement of Materials. In Energy Technologies, Vol. 1 – the Problem, its Characterization and Effects on Particular Alloy Classes.

Elsevier, New York, USA, **2012**.

(19) G. Lu and E. Kaxiras, Hydrogen embrittlement of aluminum: the crucial role of vacancies. *Phys. Rev. Lett.* **2005**, *94*, 155501.

(20) B. Bonin, M. Colin, and A. Dutfoy, Pressure building during the early states of gas production in a radioactive waste repository. *J. Nucl. Mat.* **2000**, *281*, 10.

(21) B.H. Milosavljevic and J.K. Thomas, Reactions of Electrons on the Surface of γ-Al_2O_3. A Pulse Radiolytic Study with 0.4 MeV Electrons. *J. Phys. Chem. B* **2003**, *107*, 11907.

(22) J.A. LaVerne and S.M. Pimblott, New Mechanism for H_2 Formation in Water. *J. Phys. Chem. A* **2000**, *104*, 9820.

(23) J.A. Kaddissy, S. Esnouf, D. Saffre, and J.-P. Renault, Efficient hydrogen production from irradiated aluminum hydroxides. *Int. J. Hydrogen Energy* **2019**, *44*, 3737.

(24) J.K. Thomas, Physical Aspects of Radiation-Induced Processes on SiO_2, γ-Al_2O_3, Zeolites, and Clays. *Chem. Rev.* **2005**, *105*, 1683.

(25) M. Conroy, J.A. Soltis, R.S. Wittman, F.N. Smith, S. Chatterjee, X. Zhang, E.S. Ilton, and E.C. Buck, Importance of interlayer H bonding structure to the stability of layered minerals. *Scientific Reports* **2017**, *7*, 13274.

(26) S. Le Caer, Water Radiolysis: Influence of Oxide Surfaces on H_2 Production under Ionizing Radiation. *Water* **2011**, *(3)*, 235.

(27) J. Joubert, A. Salameh, V. Krakoviack, F. Delbecq, P. Sautet, C. Coperet, and J.M. Basset, Heterolytic Splitting of H_2 and CH_4 on y-Alumina as a Structural Probe for Defect Sites. *J. Phys. Chem. B* **2006**, *110*, 23944.

(28) M. Garcia-Melchor and N. Lopez, Homolytic Products from Heterolytic Paths in H_2 Dissociation on Metal Oxides: The Example of CeO_2. *J. Phys. Chem. C* **2014**, *118*, 10921.

(29) C.D. Pilgrim, J.K. Conrad, J.R. Wilbanks, R.P. Morco, J.W. Jones, T.S. Yoder, R.E. Smith, and G.P. Horne, Milestone 1.2.11: H_2 Production from Surrogate Non-Native Corrosion Plumes on Aluminum 6061-T6 Fuel Cladding Surrogates. *INL/RPT-22-69323* **2022**.

(30) P. Winston, S. Middlemas, A. Winston, J. Aguiar, X. Liu, and K. Tolman, Aluminum Spent Fuel Performance in Dry Storage Task 4 Aluminum Oxide Sampling of ATR Dry-Stored Fuel. *INL/EXT-20-58404* **2020**.

(31) P.L. Huestis, C.I. Pearce, X. Zhang, A.T. N'Diaye, K.M. Rosso, J.A. LaVerne, Radiolytic stability of gibbsite and boehmite with adsorbed water. *J. Nucl. Mater.* **2018**, *501*, 224

(32) Z.M. Wang, E.D. Walter, M. Sassi *et al.* The role of surface hydroxyls on the radiolysis of gibbsite and boehmite nanoplatelets. *J. Hazard. Mater.* **2020,** *398*, 122853.

(33) C. Verst, A. d'Entremont, B. Radnall, J. McNamara, J. Jarrell, and R. Sindelar, Interim Irradiation and Measurement of As-Dried vs As-Corroded Hydrated Oxide Specimens (Large Coupons). *SRNL-L6000-2021-00006* **2021**.

(34) J. Perry, R. Demuth, N. Cooper, T. Knight, N. Parisi and G. Stafford; A.W. Abboud, and R.E. Smith, Engineering-Scale Drying of Aluminum-Clad Spent Nuclear Fuel, *INL/EXT 21 62416* **2021**.

(35) C. Verst, MINI-CANISTER RADIOLYSIS RESULTS – PRELIMINARY RESULTS OF ALTERNATE DRYING RECIPE. *SRNL-L3110-2022-00004* **2022**.

(36) H. Fricke and E.J. Hart, The Oxidation of Fe^{2+} to Fe^{3+} by the Irradiation with *X*-Rays of Solutions of Ferrous Sulfate in Sulfuric Acid. *J. Chem. Phys.* **1935**, *3*, 60.

(37) S.D. Gates-Rector, T.N. Blanton, The Powder Diffraction File: A Quality Materials Characterization Database. *Powder Diffr.* **2019**, *34*, 352.

(38) W.J. Fu, C.D. Wei, J. Zuo, J.P. Zhang, J.Y. Zhang, S.N. Xu, A Facile Temperature-Controlled "Green" Method to Prepare Multi-kinds of High-Quality Alumina Hydrates via a Ga-In-Sn-Alloyed Aluminum-Water Interface Reaction. *ACS Omega* **2022**, *7 (23)*, 19775.

(39) X.L. Du, X.H. Su, Y.Q. Wang, J.G. Li, Thermal decomposition of grinding activated bayerite. *Mater. Res. Bull.* **2009**, *44 (3)*, 660.

(40) N. Koga, T. Fukagawa, H. Tanaka, Preparation and thermal decomposition of synthetic bayerite. *J. Therm. Anal. Calorim*. **2001**, *64 (3)*, 965.

(41) F.A. Selim, Positron annihilation spectroscopy of defects in nuclear and irradiated materials, a review, *Mater. Charact.* **2021**, 174.

(42) M. Šob, J. Kočik, J. Pavlovský, M. Pahutová, Positron annihilation study of radiation damage in neutron-irradiated zirconium and its alloys, *Mater. Sci. Eng.* **1989**, *A122*, 243.

(43) K. Dawi, C.-W. He, M.F. Barthe, P. Desgardin, A. Volgin. Vacancy defects study in Fe based alloys induced by irradiation under various conditions. *J. Phys.: Conf. Ser.* **2014**, *505 (1)*, 012007.

(44) N. Otsu, A Threshold Selection Method from Gray-Level Histograms. *IEEE Trans. Syst. Man Cybern.* **1979,** *9 (1)*, 62.